Nano Research

Open Access

Research Article

Magnetic dielectric loss synergistic mechanism and wave absorption-corrosion dual functionality of ZnSe/CoSe@CNF multicomponent composites

Qi Li[1,§], Zhenguo Gao[2,§], Wancong Zhou[1,§], Shihao Yang[1], Zirui Jia[1]✉, and Guanglei Wu[1]✉

[1] College of Materials Science and Engineering, College of Chemistry and Chemical Engineering, Qingdao University, Shandong Key Laboratory of Low Dimensional Materials and Polymer Composites, Qingdao 266071, China
[2] Nanotechnology Center, School of Fashion and Textiles, The Hong Kong Polytechnic University, Hong Kong 999077, China
§ Qi Li, Zhenguo Gao, and Wancong Zhou contributed equally to this work.

Cite this article: *Nano Research*, **2026**, *19*, 94908525. https://doi.org/10.26599/NR.2026.94908525

ABSTRACT: With the widespread adoption of electronic devices and communication technologies, electromagnetic radiation issues have become increasingly prominent. Traditional wave-absorbing materials can no longer meet current demands. This study addresses the challenge of single-component materials having a limited loss mechanism by adopting a dielectric-magnetic synergy strategy to prepare a multi-component ZnSe/CoSe@CNF (ZCSF) composite, achieving excellent electromagnetic wave absorption (EMA). The continuous conductive network constructed by carbon nanofibers (CNF) and the favorable conductivity of ZnSe significantly enhance dielectric loss, while CoSe effectively improves magnetic loss. The synergy among multiple components enables efficient matching of dielectric and magnetic losses. The results show that the Z_2CSF-3 composite exhibits outstanding EMA performance, with a minimum reflection loss and maximum effective absorption bandwidth reaching −56.58 dB and 7.60 GHz, respectively. By combining density functional theory (DFT) calculations with computer simulation technology (CST) simulations, the multi-component synergistic loss mechanism was theoretically validated to enhance EMA performance, confirming that this material can serve as a high-performance electromagnetic wave (EMW) absorber. This research provides an effective strategy for designing high-performance multi-component EMA materials through dielectric-magnetic synergy effects.

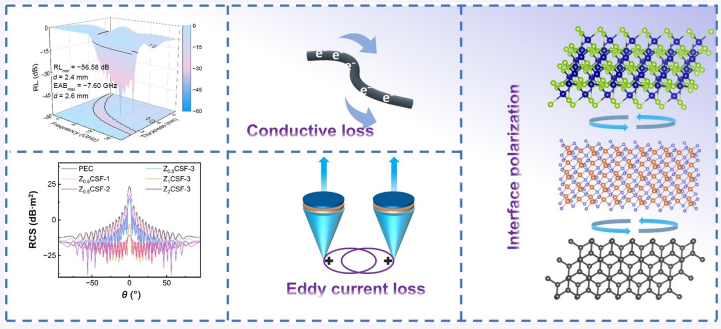

KEYWORDS: multi-component materials, electrostatic spinning, dielectric-magnetic synergistic effect, density functional theory (DFT)

1 Introduction

With the development of technology, electronic devices, communication systems and radar technology have been widely applied in daily life. A large amount of electromagnetic radiation not only interferes with the normal operation of precision electronic instruments, but also may pose a potential threat to human health [1–3]. Single-component materials are constrained by a singular loss mechanism. For instance, the intrinsic conductivity of most selenides is relatively weak, making it difficult to form a continuous conductive network to enhance dielectric loss. The electromagnetic wave absorption (EMW) loss of carbon-based materials originates from dielectric loss and lacks coordination with the magnetic loss mechanism, resulting in poor impedance matching characteristics of the materials and making it difficult to meet the requirements of the complex electromagnetic environment needed for efficient absorbing agents [4, 5]. Therefore, to overcome this scientific challenge, it is imperative to construct multi-component heterogeneous composite systems to compensate for the shortcomings of single-component materials, thereby achieving superior EMA performance [6].

Received: December 24, 2025; **Revised:** January 26, 2026
Accepted: February 2, 2026

✉Address correspondence to Zirui Jia, jiazirui@qdu.edu.cn; Guanglei Wu, wuguanglei@qdu.edu.cn, wuguanglei@mail.xjtu.edu.cn

Dielectric-magnetic synergy strategies offer an effective pathway for enhancing EMA performance, yet current research in this field still faces several critical shortcomings that urgently need to be addressed [7–10]. On the one hand, the matching mechanism of the magnetic components is still unclear, making it difficult to achieve the optimal balance between impedance matching and energy loss. As a result, even though composite materials exhibit dielectric-magnetic synergistic effects, the improvement in their wave-absorbing performance is often limited. On the other hand, achieving precise control over the interfaces in multi-component composites presents a significant challenge. Interfacial defects or impedance mismatch between the dielectric and magnetic phases is prone to occur, which may reduce the EMA efficiency. Most current studies have flaws in the construction of specific multi-component dielectric-magnetic composite systems. They lack efficient composite strategies for carbon-based conductive networks and metal selenides, and it is also difficult to achieve the synergy of dielectric and magnetic loss [11–13]. Therefore, advancing the application of dielectric-magnetic synergy strategies requires clarifying the component matching mechanism and precisely tuning the interfacial microstructure. Such approaches can strengthen the synergistic coupling between dielectric and magnetic loss, thereby providing a feasible route toward developing high-performance dielectric-magnetic composite materials.

Metal selenides hold significant research promise in the field of EMA [14–16]. Among them, ZnSe and CoSe represent two particularly promising types of metal selenides. ZnSe exhibits excellent dielectric response characteristics, which can enhance dielectric loss through polarization relaxation and charge transfer processes. CoSe can introduce magnetic loss mechanisms such as hysteresis loss and eddy current loss by virtue of its inherent magnetism. Additionally, carbon nanofiber materials, characterized by their high specific surface area, continuous conductive network, and controllable morphology, serve as an effective substrate to address the insufficient conductivity of single-component metal selenides, thereby providing stable support for improving dielectric loss [17]. By integrating CoSe, ZnSe, and carbon nanofibers and employing a dielectric-magnetic synergy strategy, the EMA performance of multi-component composite materials can be precisely regulated through adjustments in carbonization temperature and component synergy design. Sun et al. [18] prepared $Cu_2Se/CoSe_2$@CNFs composites using a MOF-on-MOF strategy. Leveraging the complementary effects between MOF derivatives and CNFs to balance polarization loss and conduction loss, they achieved optimal impedance matching. The resulting material exhibited a minimum reflection loss (RL_{min}) of −40.74 dB and an effective absorption bandwidth (EAB) of 5.17 GHz. Therefore, the construction of multi-component composite materials provides an effective strategy for solving the problem of a single loss mechanism in traditional EMA materials and expands a new direction for the research and development of high-performance EMA materials.

In this research, ZnSe/$CoSe_2$ (ZCS) precursors were synthesized via a co-precipitation and high-temperature selenization method. Subsequently, ZnSe/CoSe@CNF (ZCSF) composites were successfully prepared through electrospinning and high-temperature carbonization. By regulating the concentration of Zn^{2+} and the carbonization temperature, the electromagnetic parameters of the composite material were optimized, ultimately achieving excellent EMA performance with both high absorption intensity and wide effective bandwidth. Experimental results demonstrate that the chemical composition and annealing temperature significantly influence the EMA capacity of the materials. The Z_2CSF-3 composite annealed at 800 °C exhibited superior EMA performance. At matching thicknesses of 2.4 and 2.6 mm, the RL_{min} and EAB_{max} reached −56.58 dB and 7.6 GHz, respectively. To investigate the impact of the multicomponent structure on EMA performance and to evaluate the material's potential as a high-performance EMA, systematic analyses were conducted using combined density functional theory (DFT) calculations and computer simulation technology (CST) simulation technology. Additionally, all materials underwent electrochemical testing to assess their corrosion resistance, analyzing their degree of corrosion in simulated marine environments. This research provides a novel perspective and approach for developing EMA materials suitable for application in complex environments.

2 Experimental section

2.1 Materials

The following chemicals were used as received: potassium hexacyanocobaltate ($K_3[Co(CN)_6]$), zinc acetate ($Zn(OAc)_2$), polyvinylpyrrolidone (PVP), selenium powder (Se), N,N-dimethylformamide (DMF, 99%), polyacrylonitrile (PAN, M_W = 150,000), and deionized water. All chemicals were of analytical grade and used without further purification.

2.2 Synthesis of ZnSe/$CoSe_2$

0.2 g of $K_3[Co(CN)_6]$ was dissolved in 20 mL deionized water and stirred thoroughly. The resulting solution was then added to a 20 mL solution containing 0.13 g $Zn(OAc)_2$ and 1.11 g PVP, followed by vigorous stirring for 30 min to obtain a homogeneous solution. The solution was allowed to age for 24 h. The product was collected by centrifugation and washed twice with water and ethanol. The obtained solid was then dried overnight in a vacuum oven at 60 °C. The white powder was mixed with Se powder in a 1:1 mass ratio, and the mixture was annealed at 600 °C for 2 h with a heating rate of 2 °C/min under a nitrogen (N_2) atmosphere, yielding the $(ZnSe)_{0.5}/CoSe_2$ powder. The samples were labeled as $Z_{0.5}$CS, Z_1CS, and Z_2CS, corresponding to zinc acetate molar ratios of 0.5: 1: 2.

2.3 Synthesis of ZnSe/CoSe@CNF

1 g of the $Z_{0.5}$CS precursor and 1 g of PAN were dissolved in 10 mL of N, N-dimethylformamide and stirred at 60 °C for 12 h to obtain a homogeneous spinning solution. The solution was then loaded into a 10 mL syringe fitted with an 18-gauge needle. Electrospinning was performed at a feed rate of 1.0 mL/h under a voltage of 18 kV, with a needle-to-collector distance of 20 cm, yielding $Z_{0.5}$CS@PANF composite fibers. The fibers were dried in a vacuum oven at 60 °C for 12 h, followed by pre-oxidation in a muffle furnace at 250 °C for 2 h with a heating rate of 2 °C/min. Subsequently, the pre-oxidized fibers were carbonized in a tubular furnace under an N_2 atmosphere, ramping to 600 °C at 5 °C/min and maintaining this temperature for 2 h to obtain $Z_{0.5}$CSF-1. Using the same procedure, $Z_{0.5}$CSF-2 and $Z_{0.5}$CSF-3 were prepared at 700 and 800 °C, respectively.

2.4 Characterization

The crystal structure of the samples was characterized by X-ray

diffraction (XRD) (wavelength λ = 0.15418 nm). The morphology and structure of the samples were observed by emission scanning electron microscopy (SEM, JEOL JSM-7800F) with energy dispersion spectrometer (EDS). The lattice spacing of the samples was observed by transmission electron microscope (TEM, JEOL JEM-2100) and high-resolution transmission electron microscope (HRTEM). Raman spectroscopy at 532 nm was obtained using Renishaw InviaPlus micro-Raman spectroscopy system with a 50 mW DPSS laser. X-ray photoelectron spectroscopy (PHI5000 Versaprobe III XPS) was used to analyze the elemental composition, valence, and chemical environment of the sample. Using a vector network analyzer (Agilent N5234A, USA), the electromagnetic parameters of each sample at a test frequency of 2 to 18 GHz were measured using a coaxial method, and the EMW absorption characteristics of the sample were further calculated. Melt the sample and paraffin, and evenly disperse the sample in the paraffin matrix with a filling amount of 20 wt.%. Place the mixture into a pressing tool and press it into a ring with an inner diameter of 3.04 mm and an outer diameter of 7.00 mm. The EMW reflection loss of the material can be calculated according to the measured data of the EM parameters, calculated using the following formulas (Eqs. (1) and (2))

$$Z_{in} = Z_0\sqrt{\frac{\mu_r}{\varepsilon_r}}\tanh\left|j\left(\frac{2\pi fd}{c}\right)\sqrt{\varepsilon_r\mu_r}\right| \quad (1)$$

$$\mathrm{RL}\ (\mathrm{dB}) = 20\lg\left|\frac{Z_{in}-Z_0}{Z_{in}+Z_0}\right| \quad (2)$$

where Z_{in} and Z_0 are the input impedance of the absorber and free space, respectively. ε_r and μ_r are the complex permittivity and complex permeability of the absorber, respectively; j represents the imaginary part of the impedance. d is the thickness of the sample; f is the frequency and c is the velocity of light in free space. All samples were tested electrochemically using a CHI 660E electrochemical workstation in 1 M Na_2SO_4 solution through a typical three-electrode system. A platinum sheet was used as a counter electrode, Ag/AgCl as the reference electrode, and a platinum carbon electrode as the working electrode.

3 Result and discussion

The synthesis process of ZCSF composite materials is shown in Fig. 1(a). Firstly, ZCS was obtained through co-precipitation and high-temperature selenification. In the synthesis process, PVP was employed as a surface stabilizer and growth regulator [19], which promoted the agglomeration of the precursors into spherical

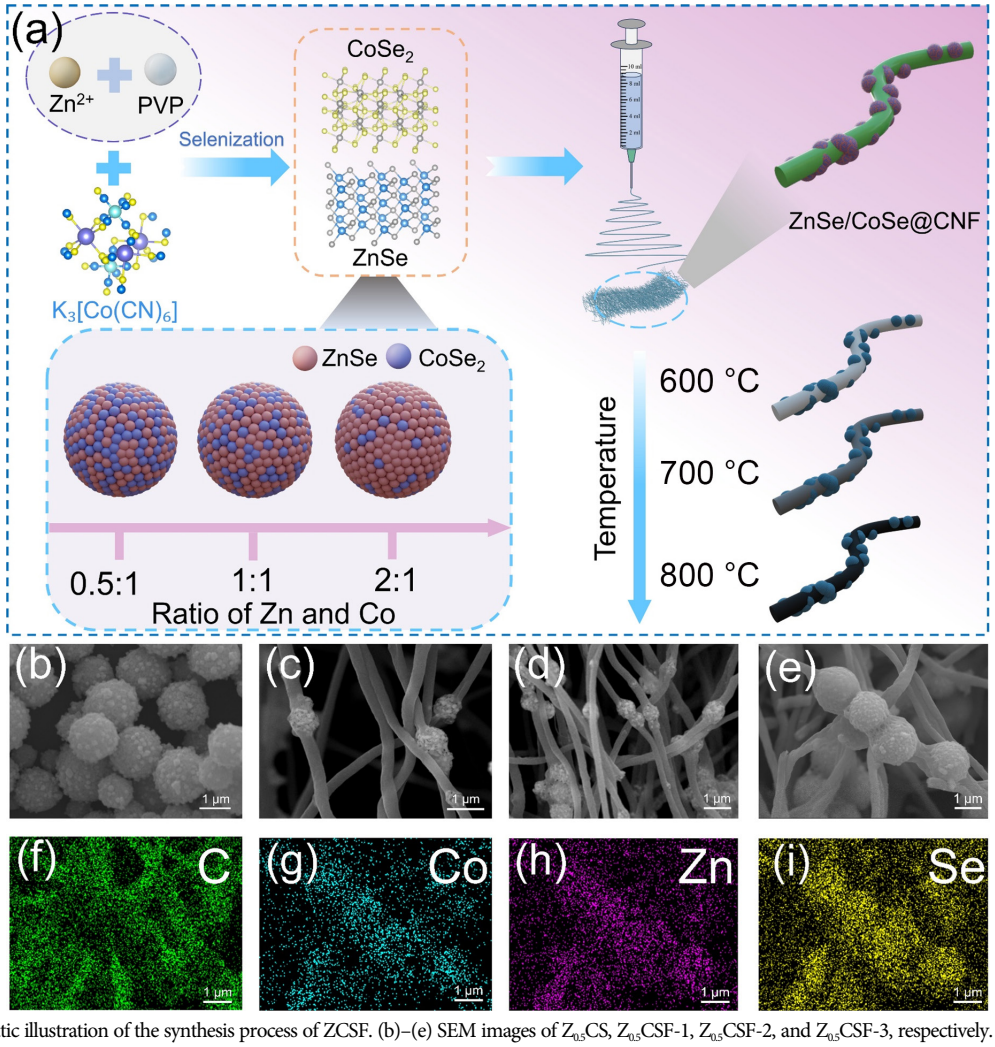

Figure 1 (a) Schematic illustration of the synthesis process of ZCSF. (b)–(e) SEM images of $Z_{0.5}$CS, $Z_{0.5}$CSF-1, $Z_{0.5}$CSF-2, and $Z_{0.5}$CSF-3, respectively. (f)–(i) EDS elemental mappings of $Z_{0.5}$CSF-3.

particles. Subsequently, the precursor was uniformly mixed with polyacrylonitrile solution, and the ZCSF composite material was obtained through electrospinning and high-temperature calcination processes. This work centers on optimizing the pyrolysis temperature and regulating the zinc-cobalt ratio. During the construction of ZCSF composite materials, multiple sets of pyrolysis temperatures were set for comparison. Variations in temperature induce differences in the carbonization degree of composite materials, which exerts a notable influence on the EMA performance of the samples. Meanwhile, by adjusting the proportion of ZnSe content, optimizing the electronic structure, carrier migration efficiency and the number of active sites of the material, the material performance is enhanced in terms of composition control, thereby influencing the EMA characteristics.

SEM was utilized to characterize the microscopic morphology and structure of the sample. Figure 1(a) and Figs. S1(a)–S1(c) in the Electronic Supplementary Material (ESM) show the SEM at different Zn^{2+} concentrations, which exhibit relatively regular spherical morphologies. These spherical particles are relatively uniform in size, with some small particles adhering to their surfaces. It can be seen that the increase in the proportion of zinc ions has an impact on the aggregation mode of the material during the reaction process, making the combination between particles tighter. The energy spectrum (EDS) image (Figs. S1(d1)–S1(d5) in the ESM) of Z_1CS shows the distribution characteristics of C, N, Zn, Co, and Se elements, which visually confirms the successful synthesis of ZCS. Figures 1(c)–1(e) and Figs. 1(f)–1(i) respectively show the SEM images of ZCSF and the EDS images of $Z_{0.5}$CSF-3 at three groups of temperatures. The material presents a fibrous morphology and forms a network-like structure. Spherical substances exist on the fiber surface, indicating that the precursor ZCS is uniformly distributed in the fibers. The successful synthesis of ZCSF composite materials has been confirmed. As the annealing temperature increases, the ZCS particles on the fiber surface adhere more tightly to the carbon nanofibers, and this trend is more distinct at 800 °C. In addition, high-temperature treatment will affect its electron transport characteristics. Due to the increase in the crystallinity of carbon atoms, the carbon atoms inside the fibers will gradually change from a disordered arrangement to a more ordered graphitized microcrystalline structure. This change will reduce the scattering resistance during the electron transport process, promote electron conduction within the fibers, and facilitate the rapid transfer of charges between the composite materials. This enhances the material's response and attenuation to EMW and other properties.

In Fig. 2(a) and Fig. S2 in the ESM, the XRD patterns of $Z_{0.5}$CS, $Z_{0.5}$CSF-1, $Z_{0.5}$CSF-2 and $Z_{0.5}$CSF-3 are shown. ZnSe (PDF #01-070-0777) corresponds to its (111), (220), (311), (400) and (331) crystal planes at 27.40°, 45.51°, 53.94°, 66.32° and 73.18°, respectively. The diffraction peaks at 30.49°, 34.19°, 37.57°, 43.66°, 51.71°, 56.59°, 58.94°, 63.46° and 74.10° correspond respectively to (200), (210), (211), (220), (311), (023), (321), (400), and (421) planes of $CoSe_2$ (PDF #03-065-3327). The diffraction peaks at 28.50°, 33.22°, 44.78°, 50.48°, 60.09°, 62.14° and 69.75° correspond respectively to (100), (101), (102), (110), (103), (112) and (202) of CoSe (PDF #01-089-2004) crystal plane. From this, the successful synthesis of the precursors ZCS and ZCSF can be determined. It should be noted that the characteristic peaks of carbon overlap with those related to highly crystalline ZCSF [20]. As the pyrolysis temperature is elevated from 600 to 800 °C, the diffraction peak around 27° gradually intensifies, which indicates that the degree of carbonization is gradually increasing. Furthermore, the XRD patterns and SEM micrographs of ZnSe@CNF, CoSe@CNF, Z_1CSF-3, and Z_2CSF-3 are displayed in Fig. S3 and S4 in the ESM, respectively. In particular, Z_1CSF-3 and Z_2CSF-3 exhibit morphology and crystal structure similar to those of $Z_{0.5}$CSF-3. Thus, the discrepancies between these samples stem primarily from variations in their chemical compositions. In Raman spectroscopy (Fig. 2(b)), the

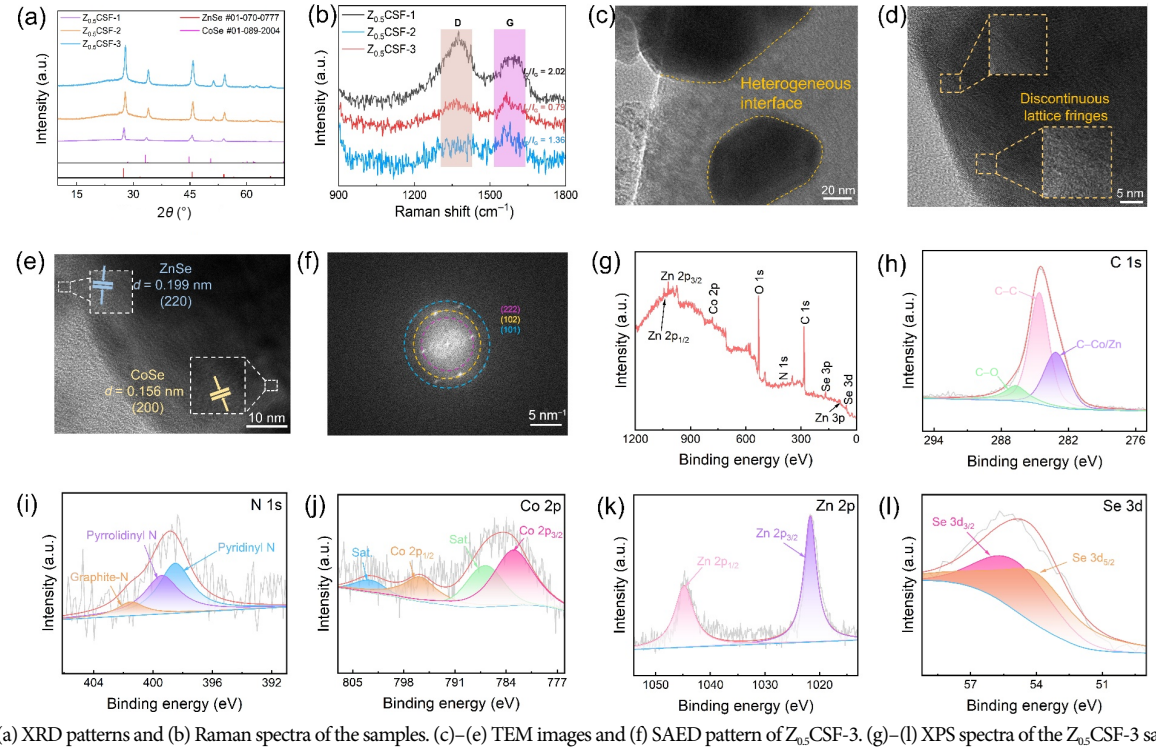

Figure 2 (a) XRD patterns and (b) Raman spectra of the samples. (c)–(e) TEM images and (f) SAED pattern of $Z_{0.5}$CSF-3. (g)–(l) XPS spectra of the $Z_{0.5}$CSF-3 samples.

intensity ratio of the 1350 and 1590 cm^{-1} peaks (I_D/I_G) serves as a metric to assess the density of internal defects and the graphitization degree of the samples [21]. The I_D/I_G of $Z_{0.5}$CSF-1, $Z_{0.5}$CSF-2 and $Z_{0.5}$CSF-3 were 2.02, 1.36 and 0.79 respectively, indicating that there were a large number of structural defects in the carbon network. Due to the gradual decrease of the value of I_D/I_G, it was further confirmed that the increase of pyrolysis temperature promoted the graphitization degree of carbon.

In Figs. 2(c) and 2(d), the presence of heterogeneous interfaces and discontinuous lattice fringes can be observed in $Z_{0.5}$CSF-3. Specifically, during the transformation stage around the ZnSe and CoSe phases, lattice mismatches may generate a large number of defects to accommodate the lattice parameter differences at the relevant interfaces [22]. Defects arising from discontinuous lattice fringes can undergo defect polarization relaxation when exposed to alternating electromagnetic fields, a process that significantly enhances the dielectric loss performance. In the HRTEM images of $Z_{0.5}$CSF-3 (Fig. 2(e)), the measured interplanar spacings were 0.199 and 0.156 nm, corresponding to the (220) crystal plane of ZnSe and the (200) crystal plane of CoSe, respectively. In Fig. 2(f), the diffraction rings are assigned to the (101) and (102) crystal planes of CoSe as well as the (222) crystal plane of ZnSe, which further verifies the successful fabrication of the target product. XPS was utilized to investigate the molecular structure and chemical states of the sample surface. As depicted in Fig. 2(g), characteristic peaks of C, N, O, Zn, Co and Se are detected within the binding energy range of 0–1200 eV. The C 1s spectrum presents three characteristic peaks at 283.1, 284.6 and 286.7 eV (Fig. 2(h)); these are assigned to the C–Co/Zn, C–C and C–O groups, correspondingly [23]. The carbon-oxygen moieties are categorized as defects within the carbon layer, and such defects are capable of inducing dipole polarization during the process of EMA [24]. The N 1s XPS spectrum is displayed in Fig. 2(i), where pyridinic nitrogen, pyrrolic nitrogen and graphitic nitrogen correspond to binding energies of 398.5, 399.4, and 401.5 eV, in that order [25, 26]. Graphitic nitrogen is able to adjust the electronic structure of carbon-based materials and accelerate electron transport, thereby enhancing conductive loss and EMA performance [27]. The Co 2p spectrum exhibits four characteristic peaks (Fig. 2(j)): the peaks at 783.0 and 795.8 eV correspond to Co^{2+} $2p^{3/2}$ and Co^{2+} $2p_{1/2}$, in that order, while the two peaks at 786.9 and 802.6 eV are attributed to the shake-up satellite peaks of Co^{2+} (designated as "Sat.") [28]. The Zn 2p energy spectrum is presented in Fig. 2(k). Characteristic peaks located at 1021.72 and 1044.8 eV are assigned to Zn $2p_{3/2}$ and Zn $2p_{1/2}$, in that order [29], demonstrating that Zn exists in the Zn^{2+} oxidation state within ZnSe. With regard to the Se 3d spectrum (Fig. 2(l)), two fitting peaks located at 54.0 and 54.9 eV (with an energy difference of 0.9 eV) were confirmed as Se $3d_{5/2}$ and Se $3d_{3/2}$ of Se^{2-}. The occurrence of Se $3d_{5/2}$ and Se $3d_{3/2}$ peaks is attributable to the generation of Zn–Se and Co–Se bonds [30, 31].

According to the EMW theory, the complex dielectric constant ($\varepsilon_r = \varepsilon' - j\varepsilon''$) and complex permeability ($\mu_r = \mu' - j\mu''$) serve as key parameters for characterizing the electromagnetic response of samples. The real component (ε') of the dielectric constant indicates the material's energy storage capability, whereas the imaginary component (ε'') denotes its energy dissipation capacity. As depicted in Figs. 3(a) and 3(b), the dielectric constant of the sample displays notable variations across the 2–18 GHz frequency range, signifying the occurrence of a prominent polarization loss mechanism. By comparing different samples, it can be found that Z_2CSF-3 exhibits the highest ε' and ε'', reflecting its excellent dielectric loss capability. Both $Z_{0.5}$CSF-3 and Z_1CSF-3 also exhibited relatively high dielectric loss values. In contrast, the ε' and ε'' of $Z_{0.5}$CSF-1, Z_1CSF-1 and Z_2CSF-1 (Fig. S5 in the ESM) carbonized at 600 °C were much lower than those of the other samples. This difference stems from the influence of annealing temperature and Zn^{2+} concentration on the microstructure of the material. With the increase of annealing temperature, ε shows an upward trend. This is because high-temperature pyrolysis enhances the graphitization degree of carbon nanofibers and promotes electron conduction within the

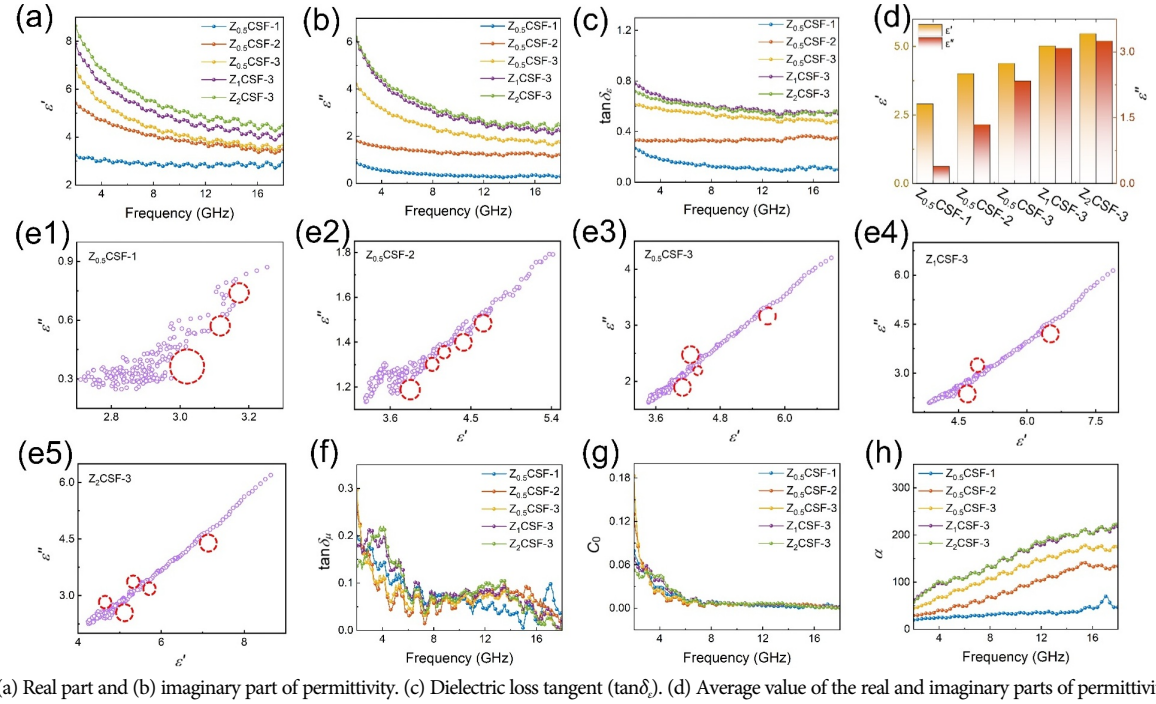

Figure 3 (a) Real part and (b) imaginary part of permittivity. (c) Dielectric loss tangent ($\tan\delta_\varepsilon$). (d) Average value of the real and imaginary parts of permittivity. (e1)–(e5) Cole–Cole plots. (f) Magnetic loss tangent ($\tan\delta_\mu$). (g) C_0 curves of the composites. (h) Attenuation constants of the composites.

fibers. In addition, as the concentration of Zn^{2+} increases, ε shows an overall upward trend. This is attributable to the fact that the dielectric properties of ZnSe are enhanced as the Zn content increases. The introduction of more ZnSe phases enhances the charge storage capacity of the material, thereby improving its dielectric loss capacity. In Fig. 3(d), the average values of the dielectric real part and the dielectric imaginary part of the sample are shown, which more intuitively demonstrates the dielectric variation trend of the material. Polarization relaxation exerts a notable influence on the EMA capability. According to Debye theory (Eqs. (3) and (4)) [32, 33]

$$\varepsilon' = \varepsilon_\infty + \frac{\varepsilon_s - \varepsilon_\infty}{1 + (2\pi f)^2 \tau^2} \tag{3}$$

$$\varepsilon'' = \frac{2\pi f\tau (\varepsilon_s - \varepsilon_\infty)}{1 + (2\pi f)^2 \tau^2} \tag{4}$$

Here, ε_s and ε_∞ denote the static permittivity and optical permittivity, respectively, while f and τ are assigned to the matching frequency and relaxation time, correspondingly. The Cole–Cole equation (Eq. (5)) is obtained from Eqs. (3) and (4) [34]

$$\left(\varepsilon' - \frac{\varepsilon_s - \varepsilon_\infty}{2}\right)^2 + (\varepsilon'')^2 = \left(\frac{\varepsilon_s - \varepsilon_\infty}{2}\right)^2 \tag{5}$$

According to Debye theory, the Cole-Cole curves (Figs. 3(e1)–3(e5)) and Fig. S6 in the ESM) exhibit multiple semi-circles within the range of 2 to 18 GHz, indicating that the material undergoes a polarization relaxation process. As the pyrolysis temperature increases, the shape distribution in the figure becomes linear. This is because elevated temperatures enhance the graphitization level of the nanofibers, thus raising the conductive loss of the samples [35]. Owing to the inclusion of magnetic nanoparticles within the samples, the values of μ' for all the samples (Fig. S7 in the ESM) range from 0.8 to 1.6, and μ'' exhibits significant fluctuations with increasing frequency, showing clear resonance peaks of μ'' at various frequencies [36], which reflects the magnetic response characteristics of these samples. In contrast, the single-component ZnSe@CNF, which contains no magnetic phase, exhibits a μ' value that remains close to 1. Generally, electromagnetic attenuation losses include dielectric losses and magnetic losses. The dielectric loss tangent ($\tan\delta_\varepsilon$) and magnetic loss tangent ($\tan\delta_\mu$) are widely used to assess attenuation losses, which significantly affect the EMA performance of microwave-absorbing materials [37]. The Z_2CSF-3 absorbing material demonstrates the highest $\tan\delta_\varepsilon$ values within the 2 to 18 GHz frequency range, which is attributed to the promotion of electron transfer by the graphitized carbon framework, and the increased ZnSe content plays a key role in the synergistic optimization of interface polarization and dielectric loss. In Fig. 3(f), the magnetic nanoparticles exhibit prominent natural and exchange resonance behaviors of $\tan\delta_\mu$ in the low-frequency and high-frequency bands owing to their greater magnetic anisotropy [38]. Additionally, it is noteworthy that in the low frequency region (2–6 GHz), a distinct resonance peak appears in $\tan\delta_\mu$, and its value is significantly higher compared to that in the mid frequency range, indicating that magnetic loss plays a crucial role in this frequency band. As the frequency increases to the mid to high frequency region (6–18 GHz), $\tan\delta_\varepsilon$ is generally higher than $\tan\delta_\mu$, indicating that dielectric loss is the predominant electromagnetic attenuation loss mechanism in the obtained ZCSF composites [39]. Therefore, the excellent broadband absorption performance of the ZCSF composite originates from the synergy and complementarity between magnetic loss in the low frequency region and dielectric loss in the mid to high frequency region, thereby constructing a broad and efficient EMW dissipation pathway.

The presence of eddy current loss is typically represented by C_0, as shown in Eq. (6)

$$C_0 = \mu''(\mu')^{-2} f^{-1} = 2\pi\mu_0 d^2\sigma \tag{6}$$

where μ_0 refers to the magnetic permeability of free space, and σ corresponds to the electrical conductivity. The category of magnetic loss mechanism may be identified by the variation trend of C_0 values with frequency; the fluctuations in the low-frequency band correspond to natural resonance [40]. It is evident from Fig. 3(g) and Fig. S8(a) in the ESM that the curve spanning 8 to 18 GHz stays comparatively stable, which demonstrates that eddy current loss constitutes the dominant source of magnetic loss. However, the curve varies notably across the 2–8 GHz range, signifying that natural resonance acts as the primary loss mechanism in the low-frequency band. Therefore, magnetic loss dissipates EMW through the synergistic action of multiple mechanisms. To attain high-performance EMA, microwave-absorbing samples need to satisfy both appropriate impedance matching ($Z = Z_{in}/Z_0$) and a favorable attenuation constant (α) [41]. The attenuation capability for incident EMW energy strengthens as the value of α increases [42]. The attenuation constants of Z_1CSF-3 and Z_2CSF-3 (Fig. 3(h)) are markedly greater than those of the other composites, signifying that these two samples possess enhanced EMW dissipation capacities. Therefore, by adjusting the annealing temperature and the concentration of Zn^{2+}, the attenuation constant of the material can be optimized, thereby enhancing the EMA performance of the material.

Figures 4(a1)–4(a5) and Fig. S9 in the ESM illustrate the EMA properties of all the samples. An ideal EMA material should have a thin thickness, a wide absorption bandwidth, and excellent reflection loss performance. The single-component materials ZnSe@CNF and CoSe@CNF exhibit RL_{min} values reaching −40 dB; however, their matching thicknesses both exceed 7.5 mm. Therefore, combining the two components is essential to further improve the microwave absorption performance of the electromagnetic material. The $Z_{0.5}$CSF-1 composite material exhibits a RL_{min} of −17.73 dB and a EAB_{max} of 1.60 GHz, with a thickness nearly reaching 8 mm, which performs relatively poorly compared to the currently published EMA materials [43–47]. To improve the absorption performance, the pyrolysis temperature and chemical composition were systematically optimized. As observed, when the pyrolysis temperature was elevated to 700 °C, the EAB of $Z_{0.5}$CSF-2 increased to 7.20 GHz, though its minimum reflection loss did not meet expectations. The temperature was further increased to 800 °C. The RL_{min} and EAB_{max} of $Z_{0.5}$CSF-3 were −56.52 dB and 7.44 GHz respectively, and the corresponding thicknesses were 4.5 and 3.0 mm respectively. However, they still failed to satisfy the low-thickness demands of the microwave-absorbing samples. Therefore, the focus should be shifted to regulating the chemical composition of the composite material, increasing the concentration of Zn^{2+} while raising the pyrolysis temperature. The results showed that the RL_{min} and EAB_{max} of Z_1CSF-3 reached −60.41 dB and 7.84 GHz respectively. For Z_2CSF-3, the RL_{min} was −56.58 dB at 2.4 mm thickness, while its EAB_{max} reached 7.60 GHz at a thickness of 2.6 mm. Moreover, Z_2CSF-3 exhibits a frequency coverage from 10 to

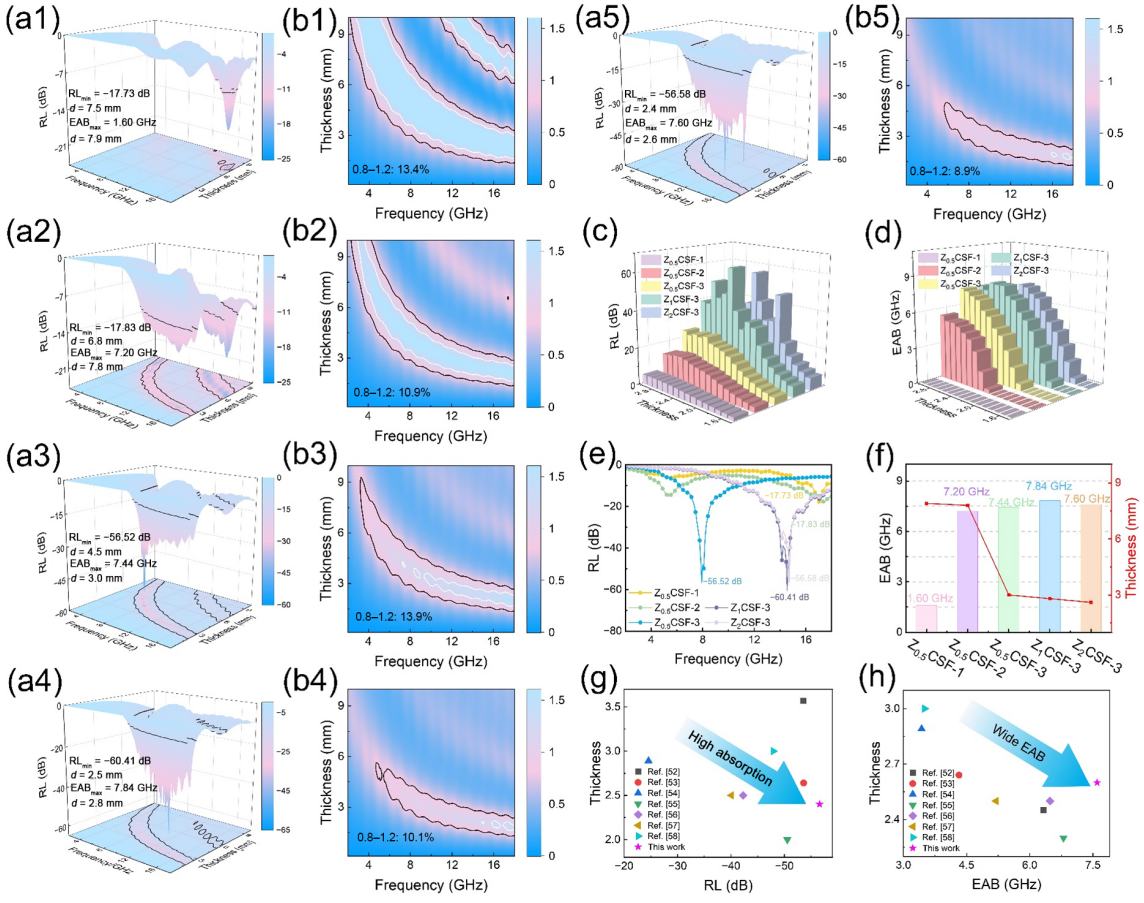

Figure 4 (a1)–(a5) 3D RL curves. (b1)–(b5) Two-dimensional impedance matching plots. (c) 3D RL curves in the thickness range of 1.5–3 mm. (d) EAB in the thickness range of 1.5–3 mm. (e) RL at the thickness corresponding to the minimum reflection loss RL_{min}. (f) EAB_{max} and its corresponding thickness. (g)–(h) Comparisons of the RL_{min} and EAB between previous works and this work.

17.52 GHz, nearly encompassing the entire Ku band, demonstrating its excellent EMA properties. The nearer the *Z* value is to 1, the more favorable the impedance matching of the sample. As shown in Fig. 4(b) and Fig. S10 in the ESM, the area of the impedance matching region within the range of 0.8 to 1.2 for all samples exceeds 8%, indicating that they have excellent impedance matching. The RL_{min} and the EAB_{max} corresponding to the $Z_{0.5}$CSF-1, $Z_{0.5}$CSF-2, $Z_{0.5}$CSF-3, Z_1CSF-3 and Z_2CSF-3 composites in the range of 1.5 to 3 mm are shown in Figs. 4(c) and 4(d). And in Figs. 4(e) and 4(f), the reflection loss at the thickness corresponding to the RL_{min} and the EAB_{max} of each sample, as well as the corresponding thickness, are visually presented. The electromagnetic absorption performance differences of various samples were systematically demonstrated from three aspects: strong wave absorption, wide frequency band and thin thickness, further verifying their outstanding EMA performance. By comparing the EMA performance of this study with that of recent cutting-edge research, the results (Figs. 4(g) and 4(h)) demonstrate that Z_2CSF-3 exhibits outstanding performance in both RL_{min} and EAB_{max}. This validates the optimization of wave absorption properties in multicomponent materials achieved through the synergistic effect of dielectric and magnetic loss [48–53].

Based on the optimized crystal structure (Figs. 5(a)–5(c)), the densities of states of ZnSe, CoSe and ZnSe/CoSe (DOS, Fig. S11(a) in the ESM) were systematically characterized through DFT calculations. With the band structure (Figs. 5(d)–5(f)). The DOS analysis results show that compared with single ZnSe and CoSe, ZnSe/CoSe bimetallic selenides exhibit a significantly enhanced electron density of states near the Fermi level, indicating that the material has superior electron transport capacity. This feature is conducive to improving the material's electrical conductivity and dielectric loss efficiency. As shown in Figs. S11(b) and S11(c) in the ESM, the Fermi level difference between ZnSe and CoSe before contact indicates that CoSe has a lower Fermi level (3.55 eV) than ZnSe (4.19 eV). The charge density difference map (Figs. 5(g)–5(i)) visually reveals strong electronic interactions between ZnSe and CoSe, and upon the formation of the heterojunction, a built-in electric field spontaneously forms at the interface, directed from ZnSe to CoSe. This built-in electric field induces the accumulation of negative charges on the CoSe side and positive charges on the ZnSe side of the interface, forming a stable interface charge separation layer. The results from the Electron Localization Function (Figs. 5(j)–5(l)) further corroborate this interfacial electron transfer behavior, providing direct theoretical support for the charge transport mechanism in the heterojunction.

To characterize the practical far-field EMA performance of the as-prepared ZCSF, a CST simulation was performed to model the three-dimensional radar wave scattering signals of a perfect electric conductor (PEC) and all samples at 14.7 GHz (Figs. 6(a1)–6(a5) and Fig. S12 in the ESM). It is evident that the radar wave scattering signal intensity of ZnSe@CNF, CoSe@CNF and Z_xCSF-1 is moderately reduced relative to PEC, whereas that of Z_xCSF-2 has

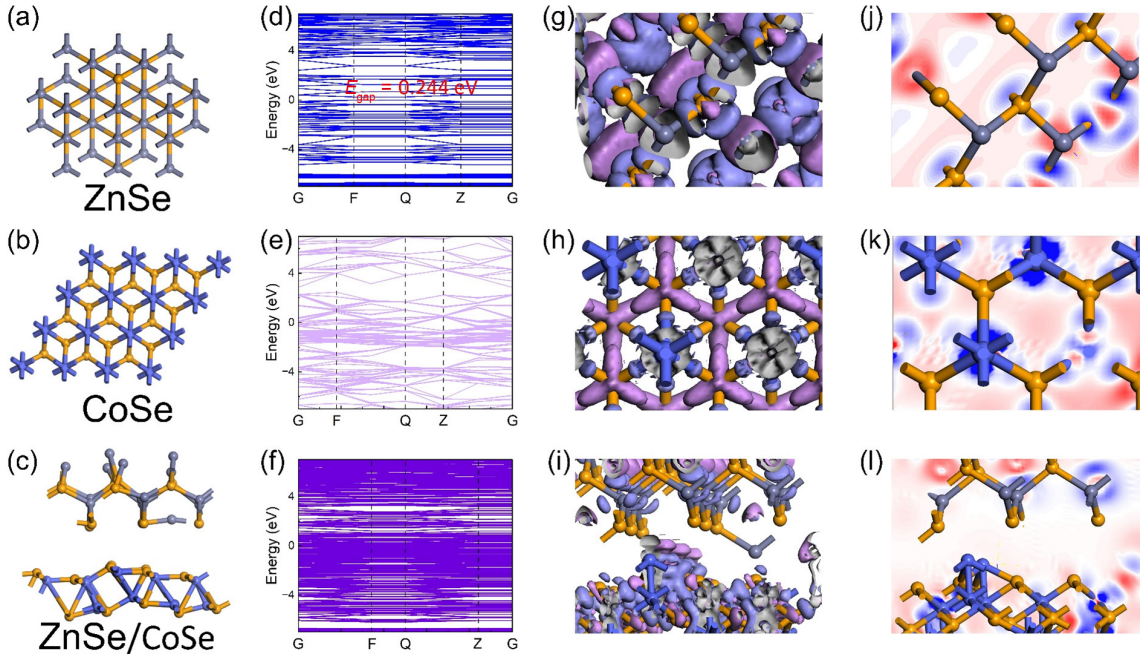

Figure 5 Crystal structures of (a) ZnSe, (b) CoSe, and (c) ZnSe/CoSe. Electronic band structures of (d) ZnSe, (e) CoSe, and (f) ZnSe/CoSe. Corresponding partial charge density distributions of (j) ZnSe, (k) CoSe, and (l)ZnSe/CoSe.

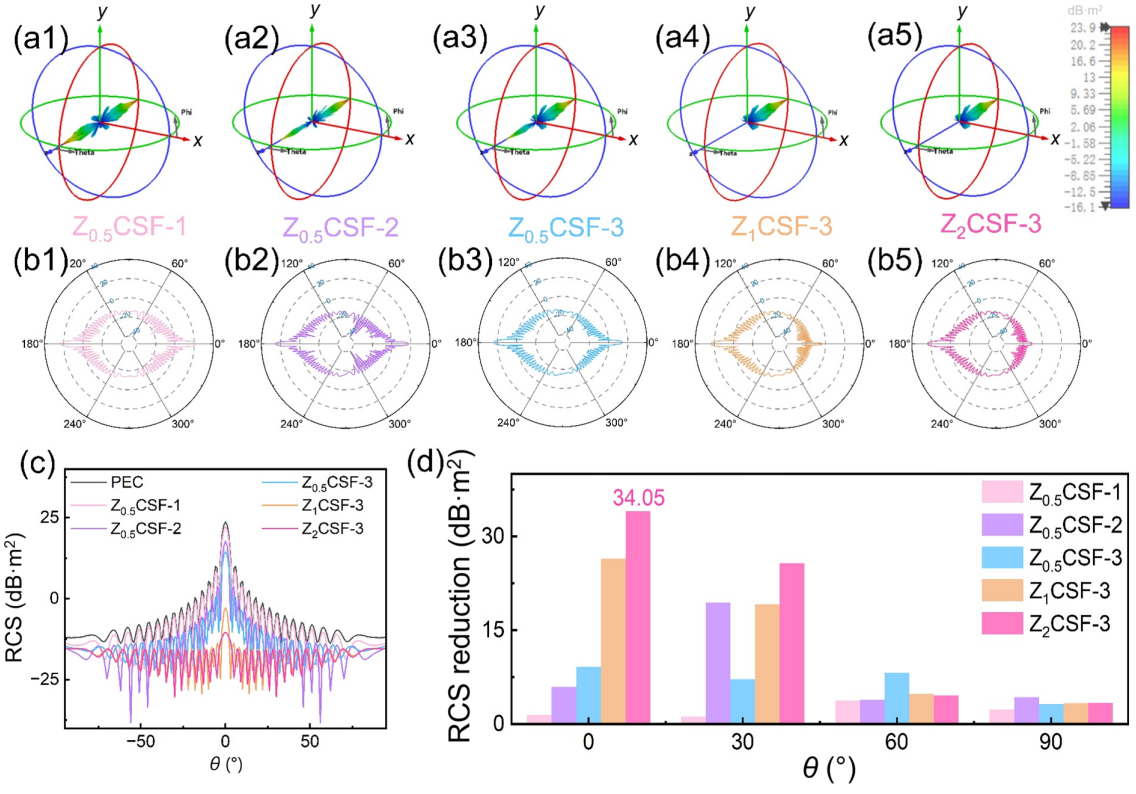

Figure 6 (a1)–(a5) 3D radar wave scattering signals of samples. (b1)–(b5) RCS simulation results of polar coordinates of $Z_{0.5}$CSF-1, $Z_{0.5}$CSF-2, $Z_{0.5}$CSF-3, Z_1CSF-3, and Z_2CSF-3, respectively. (c) RCS simulation curves. (d) RCS reduction value of the samples.

exhibited a substantial decline. It is worth noting that the radar scattering signal intensity of Z_2CSF-3 is the lowest after increasing the pyrolysis temperature, indicating that its EMW attenuation ability is relatively strong. The key indicator for measuring the scattering ability of a target to radar EMW is the radar cross section (RCS). The lower the RCS value, the superior the radar stealth capability of the target. Figures 6(b) and 6(c) and Fig. S13 in the ESM show the RCS of all samples from different angles. Obviously, the RCS curves of all samples were significantly lower than PEC, indicating that this composite material, through the combined effects of electromagnetic loss, structural scattering, etc., greatly suppressed radar scattering across the entire angle range. To further

reflect the stealth performance of the samples, the reduction of RCS at four angles (0°, 30°, 60°, and 90°) was analyzed. The decrease in Z_2CSF-3 was the most significant, achieving a reduction in RCS of 34.05 dB·m^2 at 0° (Fig. 6(d)), which was much higher than that of other samples. Therefore, this further proves that ZCSF can become an EMW absorber with a powerful EMA capacity.

The multi-scale EMA mechanism of ZCSF composite materials is shown in Fig. 7(a). When incident EMW interact with the sample, they repeatedly alter their propagation direction within the fiber voids and across the surfaces of heterogeneous particles in the sample. This notably extends the EMW transmission path inside the sample and facilitates EMA. The conductive property of ZnSe itself and the continuous conductive network constructed by carbon fibers will cause the free electrons within the material to move along the conductive network under the drive of alternating EMW. During the migration process, the electrons interact with the lattice, defects, etc., converting electromagnetic energy into thermal energy. This significantly enhances the conductive loss capacity of the material [54]. It should be emphasized that ZCSF contains numerous heterogeneous interfaces. The substances on both sides of these interfaces have different dielectric constants and conductivities. Under the excitation of alternating EMW, the multiple heterogeneous interfaces within the sample facilitate the accumulation of positive and negative charges at the interface regions. This induces polarization relaxation, which in turn enhances the dielectric loss capability of the sample for EMA. When the material is in an electromagnetic field, the interface charges are difficult to respond synchronously to the alternating rhythm of the EMW. Meanwhile, the incorporation of magnetic metal nanoparticles imparts magnetism to the composite, allowing it to dissipate EMW via magnetic response mechanisms [55–57]. Alternating electromagnetic fields can induce eddy current losses within materials, further dissipating electromagnetic energy. In summary, ZCSF composite materials achieve EMA through the synergistic effect of multiple loss mechanisms, and through this coordinated multiple loss mode, ultimately achieve a wideband absorption effect of 2 to 18 GHz.

In the practical marine engineering applications of EMA materials, the seawater corrosion resistance of the materials is of vital importance. We investigated the corrosion resistance of all samples by using the electrochemical measurement technology of a three-electrode system. Figure 7(b) and Fig. S14(a) in the ESM show the changes in open-circuit potential (OCP) of the material under the variation of soaking time. Generally speaking, the higher the OCP value, the lower the corrosion tendency [58–62]. Among them, the OCP values of Z_1CSF-3 and Z_2CSF-3 were significantly higher than those of other samples, indicating that their corrosion resistance was the best. As depicted in the Nyquist plots (Fig. 7(c) and Fig. S14(b) in the ESM), the diameter of the capacitive arc is indicative of the material's corrosion resistance, where a larger arc diameter corresponds to enhanced corrosion resistance performance. ZnSe@CNF, CoSe@CNF, and Z_2CSF-3 all exhibited large diameters, indicating their excellent corrosion resistance. Figure 7(d) shows the Tafel curves, from which the corrosion potential (E_{corr}) and corrosion current density (I_{corr}) of all samples were calculated, as shown in Table S1 in the ESM. A larger corrosion potential indicates better corrosion resistance, while a higher corrosion current density implies weaker self-protection ability of the material. The E_{corr} and I_{corr} of Z_2CSF-3 are −0.196 V and 0.751×10^{-6} (A/cm^2), respectively, indicating its good corrosion resistance. The variation in the material composition and the subsequent formation of graphite carbon are the primary reasons for the differences in I_{corr} and E_{corr} values across the samples. These discrepancies arise from the differential catalytic activities of the internal components [63]. The changes in coating performance were analyzed by studying the phase Angle variations of each coating (Fig. 7(e) and S14(d) in the ESM). The results revealed that the phase angle values of each specimen were comparatively large. This suggests that the microwave-absorbing material exhibits favorable capacitive behavior and a certain degree of corrosion resistance [64, 65]. In corrosion electrochemistry research, the impedance modulus at 0.01 Hz (denoted as $|Z|_{0.01}$ Hz) is commonly employed as a semi-quantitative metric to characterize the system's

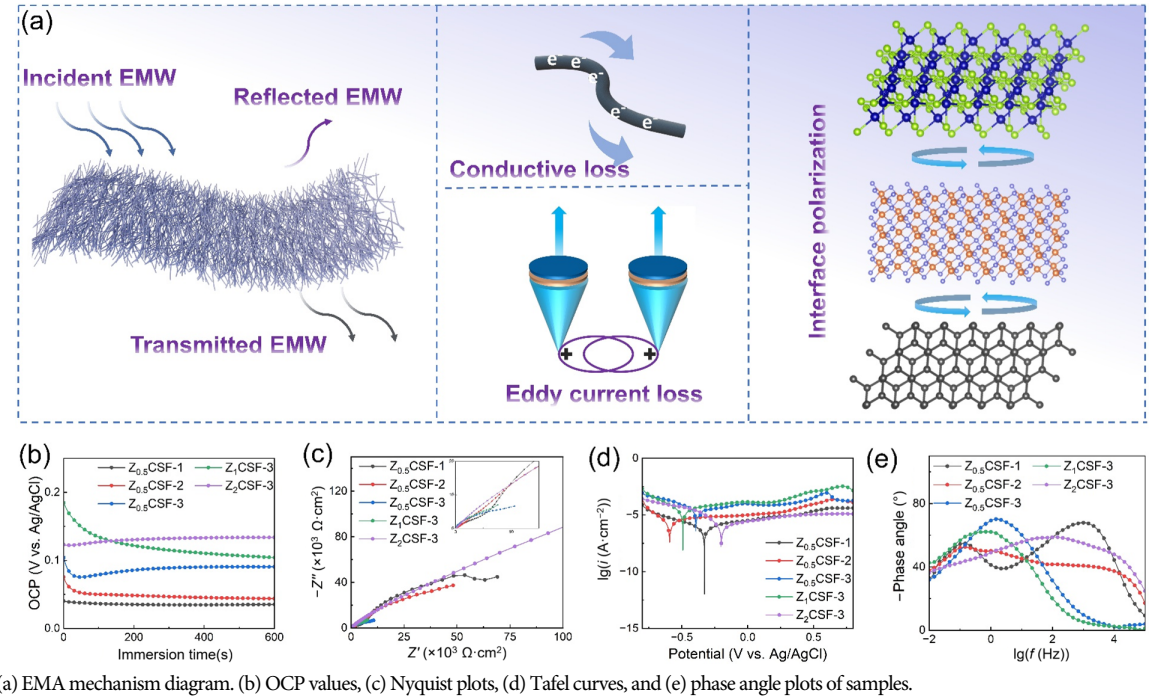

Figure 7 (a) EMA mechanism diagram. (b) OCP values, (c) Nyquist plots, (d) Tafel curves, and (e) phase angle plots of samples.

impedance magnitude, and thus assess its corrosion resistance in aggressive media [66]. The greater the magnitude of $|Z|_{0.01}$ Hz, the superior the corrosion resistance of the specimen. In Fig. S15 in the ESM, the impedance modulus of the Z_2CSF-3 composite coating is the largest, indicating that it has the strongest barrier ability against corrosive substances. Metal selenide nanoparticles are uniformly dispersed in carbon nanofibers, exerting an active anti-corrosion function. In addition, after annealing treatment at 800 °C, the PAN precursor is transformed into a dense graphitized carbon nanofiber network. Its continuous fibrous structure can form a complete physical barrier on the substrate surface, reducing the direct contact between the medium and the substrate surface. Meanwhile, the excellent chemical stability of carbon nanofibers makes them less prone to degradation in corrosive environments, ensuring the long-term integrity of the barrier layer. However, excessively high temperatures increase the brittleness of fibers, making them prone to microcracks, which in turn weakens the barrier effect and reduces their corrosion resistance [67]. The combination of uniformly dispersed metal selenide nanoparticles with a carbon network may equip the material with multiple protective mechanisms, including physical shielding and chemical passivation. Their synergistic effect offers greater reliability compared to single-component coatings. The ZCSF material exhibits both broadband EMA and excellent corrosion resistance, making it suitable for use in marine equipment, aerospace vehicles, and electronic device housings in coastal or chemical industrial areas. Its corrosion resistance directly addresses environmental erosion such as humidity, while its EMA functionality simultaneously provides electromagnetic shielding and reduces the radar cross-section. Therefore, through the synergistic design of composition and structure, this material not only achieves enhanced performance but also demonstrates application potential in complex and harsh environments, laying a foundation for the development of new-generation multifunctional protective materials.

4 Conclusions

In this study, ZCSF composite material was successfully prepared via electrospinning and high-temperature carbonization using ZCS as the precursor. The EMA mechanism and corrosion resistance of the materials were systematically discussed. The establishment of a conductive network by carbon fibers and the excellent conductivity of ZnSe significantly enhance dielectric loss. The presence of CoSe magnetic metal nanoparticles enables the composite material to dissipate EMW through magnetic loss. Based on the above dielectric-magnetic synergy mechanism of multi-component materials, ZCSF composite materials possess excellent EMA performance and corrosion resistance. By combining DFT calculations with CST simulation, the influence of multi-component materials on the EMA performance was verified at the theoretical level, and it was confirmed that this material can be used as a high-performance EMA. Meanwhile, electrochemical tests have shown that the coating with Z_2CSF-3 composite material has excellent corrosion resistance, providing a new research direction for the development of absorbing materials that combine excellent EMA performance and corrosion resistance.

Electronic Supplementary Material: Supplementary material (heoretical simulation steps, scanning images, XRD patterns, electromagnetic parameters and 3D performance, work function, RCS, and electrochemical test data graphs and charts) is available in the online version of this article at https://doi.org/10.26599/NR.2026.94908525.

Data availability

All data needed to support the conclusions in the paper are presented in the manuscript and the Electronic Supplementary Material. Additional data related to this paper may be requested from the corresponding author upon request.

Acknowledgements

We are thankful for financial support from the National Natural Science Foundation of China (Nos. 52377026 and 52301192), Taishan Scholars and Young Experts Program of Shandong Province (No. tsqn202103057), the Natural Science Foundation of Shandong Province (Nos. ZR2024ME046 and ZR2024QE313), the Postdoctoral Science Foundation of China (No. 2024M761554), and Undergraduate Innovation and Entrepreneurship Training Program Funding Project (Nos. 202511065064 and S202511065152).

Declaration of competing interest

All the contributing authors report no conflict of interests in this work.

Author contribution statement

Q. L. and Z. G. G.: Validation, writing manuscript. W. C. Z.: Data curation. S. H. Y.: Data curation. Z. R. J. and G. L. W.: Project administration, review manuscript. All the authors have approved the final manuscript.

Use of AI statement

None.

References

[1] Song, S. X.; Zheng, B. Y.; Chen, L. H.; Shu, H. M.; Gao, D. T.; Lan, D.; Li, T. X.; Liu, X.; Ma, Y. Fabrication of ZnCoM (M = Al, Ni, Fe) layered double hydroxide materials for high-performance asymmetric supercapacitors. *J. Energy Storage* **2025**, *134*, 118282.

[2] Zhou, J. X.; Huang, X. M.; Lan, D.; Jia, Z. R.; Wu, G. L. Multi-interface polarization engineering constructs one-dimensional carbon nanocages heterostructures for efficient electromagnetic wave absorption. *Carbon* **2026**, *248*, 121143.

[3] Ren, X. Y.; Jia, Z. R.; Gao, Z. G.; Zhang, S. Y.; Zhang, Y.; Lan, D.; Wu, G. L. Synergistic band and multiscale hybrid engineering in polycrystalline TiO_2 for enhanced spatial charge polarization relaxation. *Adv. Funct. Mater.* **2026**, *36*, e24264.

[4] Han, M. J.; Jia, Z. R.; Lan, D.; Gao, Z. G.; Wu, G. L. Bimetallic hybridization induced multi-polarization loss in multi-phase solid solution for electromagnetic wave absorption. *Chin. J. Chem.* **2026**, *44*, 1525–1538.

[5] Su, X. G.; Wang, J.; Liu, T.; Zhang, Y.; Liu, Y. N.; Zhang, B.; Liu, Y. Q.; Wu, H. J.; Xu, H. X. Controllable atomic migration in microstructures and defects for electromagnetic wave absorption enhancement. *Adv. Funct. Mater.* **2024**, *34*, 2403397.

[6] Lian, Y. L.; Yu, H.; Wang, M. Y.; Yang, X. N.; Li, Z.; Yang, F.; Wang, Y.; Tai, H. L.; Liao, Y. L.; Wu, J. Y. et al. A multifunctional wearable e-textile via integrated nanowire-coated fabrics. *J. Mater. Chem. C* **2020**, *8*, 8399–8409.

[7] Hu, T.; Lan, D.; Wang, J.; Zhong, X. Z.; Bu, G. X.; Yin, P. F. Construction of $NiCo_2O_4$/$NiCoO_2$ co-embedded porous bio-carbon with rich heterogeneous interfaces for excellent bacteriostatic microwave radiation protection. *Carbon* **2025**, *232*, 119798.

[8] Gao, S. T.; Zhang, Y. C.; Zhang, X. Z.; Jiao, F. C.; Liu, T.; Li, H. X.; Bai, Y. H.; Wu, C. L. Synthesis of hollow $ZnFe_2O_4$/residual carbon from coal gasification fine slag composites for multiband electromagnetic wave absorption. *J. Alloys Compd.* **2023**, *952*, 170016.

[9] Pan, Y. L.; Yu, K. L.; Lan, D.; Zhang, Z. L.; Chen, Z. S. Multiple selenide modified carbon fibers to construct heterogeneous interfaces for electromagnetic wave absorption. *Carbon* **2025**, *245*, 120824.

[10] Qi, J. M.; Liang, C. B.; Ruan, K. P.; Li, M. K.; Guo, H.; He, M. K.; Qiu, H.; Guo, Y. Q.; Gu, J. W. Cactus-like architecture for synergistic microwave absorption and thermal management. *Natl. Sci. Rev.* **2025**, *12*, nwaf394.

[11] Li, H. S.; Wu, A. M.; Qiu, Z. W.; Li, J. Z.; Wu, Z. J.; Ma, Y. C.; Wang, J.; He, S. Z.; Huang, H. Carbonization of Ni@SiC@C nanoparticles reinforced PAN nanofibers for adjustable impedance matching. *Chem. Eng. J.* **2023**, *476*, 146582.

[12] McCord, M. R. Y.; Zimmerman, J. B.; Rojas, O. J. Harnessing multifunctional electrospun nanofibers containing phase change materials for energy-efficient thermal management: A review on recent trends. *Nano Energy* **2024**, *131*, 110212.

[13] Wang, Z. X.; Jia, Z. R.; Ren, J. W.; Wang, L.; Lan, D.; Zhang, S. Y.; Shi, X. T.; Liu, X. H.; Gao, Z. G.; Wu, G. L. Multi-topological network engineering of Co/MnO composites for electromagnetic wave absorption. *J. Mater. Sci. Technol.* **2025**, *235*, 81–90.

[14] Cao, X. H.; Wu, X. Y.; Wang, X.; Luo, J. M.; Zhang, Z.; Xue, Y.; Zhang, G. L.; Zhang, L. Y.; Zhang, H.; Yu, J. Y. Mechanistic insights into the structural evolution of ZIF-67 via electrospinning strategy toward high electromagnetic wave absorption performance of ZIF-67-derived carbon nanofibers. *Adv. Sci.* **2025**, *12*, 2502560.

[15] Jiang, B.; Shang, J. X.; Zhang, F. Y.; Li, N.; Wang, Y.; Hu, Z. M.; Yu, J. R. Electrospinning fabrication of hollow C@TiO_2/Fe_3C nanofibers composites for excellent wave absorption at a low filling content. *Chem. Eng. J.* **2024**, *495*, 153663.

[16] Wang, S. J.; Zhang, X.; Hao, S. Y.; Qiao, J.; Wang, Z.; Wu, L. L.; Liu, J. R.; Wang, F. L. Nitrogen-doped magnetic-dielectric-carbon aerogel for high-efficiency electromagnetic wave absorption. *Nanomicro Lett.* **2024**, *16*, 16.

[17] Luo, Y.; He, Q. C.; Wang, Y. Q.; Yin, X. M. Preparation and electromagnetic waves absorption performance of novel Fe_3Si/SiC/SiO_2 composites. *J. Alloys Compd.* **2024**, *1003*, 175617.

[18] Sun, Y.; Wang, Y. X.; Li, Y. F.; Dai, S. C.; Ding, B. H.; Guo, J. H.; Yuan, Y. R.; Zhang, D.; Liu, D. M. MOF-introduced Cu_2Se/$CoSe_2$ and carbon nanofibers: Complementary regulation of dielectric loss for enhanced electromagnetic wave absorption. *Diamond Relat. Mater.* **2025**, *159*, 112842.

[19] Koczkur, K. M.; Mourdikoudis, S.; Polavarapu, L.; Skrabalak, S. E. Polyvinylpyrrolidone (PVP) in nanoparticle synthesis. *Dalton Trans.* **2015**, *44*, 17883–17905.

[20] Xiao, Y.; Miao, Y.; Wan, S.; Sun, Y. K.; Chen, S. M. Synergistic engineering of Se vacancies and heterointerfaces in zinc-cobalt selenide anode for highly efficient Na-ion batteries. *Small* **2022**, *18*, 2202582.

[21] Feng, A. L.; Liu, L.; Liu, P. T.; Zu, Y. Q.; Han, F. B.; Li, X. D.; Ding, S. J.; Chen, Y. A. Interfacial nanoparticles of Co_2P/Co_3Fe_7 encapsulated in N-doped carbon nanotubes as bifunctional oxygen electrocatalysts for rechargeable zinc-air batteries. *Mater. Today Energy* **2024**, *44*, 101626.

[22] Qin, M.; Zhang, L. M.; Zhao, X. R.; Wu, H. J. Defect induced polarization loss in multi-shelled spinel hollow spheres for electromagnetic wave absorption application. *Adv. Sci.* **2021**, *8*, 2004640.

[23] Jeong, S. Y.; Cho, J. S. Porous hybrid nanofibers comprising ZnSe/$CoSe_2$/carbon with uniformly distributed pores as anodes for high-performance sodium-ion batteries. *Nanomaterials* **2019**, *9*, 1362.

[24] Jiang, W. H.; Xu, S.; Lv, C. P.; Lan, D.; Zhang, S. Y.; Gao, Z. G.; Jia, Z. R.; Wu, G. L. Multi-scale engineering of N-doped carbon nanofibers with Co_3O_4/CeO_2 heterostructures: Tailoring heterointerface polarization for microwave absorption. *Carbon* **2025**, *245*, 120784.

[25] An, R. F.; Niu, H. K.; Tan, Q.; Liu, Z. W.; Gao, B. L. Enhancing sodium-ion battery performance with MXene@$CoSe_2$/ZnSe@NC 0D-2D micro-/nanostructures. *J. Energy Storage* **2024**, *82*, 110526.

[26] Zhang, Q.; Chen, M. L.; Wang, J.; Zhao, C. F.; Cao, F. H.; Li, H.; Cong, H. P.; Zhang, C. L. Ultrafine ZnSe/CoSe nanodots encapsulated in core-shell MOF-derived hierarchically porous N-doped carbon nanotubes for superior lithium/sodium storage. *J. Mater. Chem. A* **2023**, *11*, 5056–5066.

[27] Rao, L. J.; Li, Z. L.; Qian, Y. T.; Huang, M. Q.; Wang, L.; Liu, Y. S.; Zhang, J. C.; Lai, Y. X.; Liang, C. Y.; Che, R. C. Heterointerface engineering in porous microspheres for magnetic-dielectric balance to boost electromagnetic wave absorption. *Chem. Eng. J.* **2024**, *488*, 150955.

[28] Lu, M. X.; Liu, C.; Li, X. Y.; Jiang, S. Q.; Yao, Z. J.; Liu, T. C.; Yang, Y. F. Mixed phase Mo-doped $CoSe_2$ nanosheets encapsulated in N-doped carbon shell with boosted sodium storage performance. *J. Alloys Compd.* **2022**, *922*, 166265.

[29] Zhang, T.; Qiu, D. P.; Hou, Y. L. Free-standing and consecutive ZnSe@carbon nanofibers architectures as ultra-long lifespan anode for flexible lithium-ion batteries. *Nano Energy* **2022**, *94*, 106909.

[30] Shi, M. J.; Jia, Z. R.; Lan, D.; Gao, Z. G.; Zhang, S. Y.; Wu, G. L. Type-II heterojunction regulated BIEF toward nitride/chalcogenide semiconductors for multi-polarization relaxation. *Adv. Funct. Mater.* **2026**, *36*, e28665.

[31] Hong, Y. J.; Kim, J. H.; Kang, Y. C. Sodium-ion storage performance of hierarchically structured $(Co_{1/3}Fe_{2/3})Se_2$ nanofibers with fiber-in-tube nanostructures. *J. Mater. Chem. A* **2016**, *4*, 15471–15477.

[32] Wu, N. N.; Zhao, B. B.; Lian, Y. Y.; Liu, S. S.; Xian, Y.; Gu, J. W.; Wu, G. L. Metal organic frameworks derived Ni_xSe_y@NC hollow microspheres with modifiable composition and broadband microwave attenuation. *Carbon* **2024**, *226*, 119215.

[33] Zhang, Z. H.; Sun, S. S.; Xu, Z. H.; Yin, S. G. Multicomponent hybridization transition metal oxide electrode enriched with oxygen vacancy for ultralong-life supercapacitor. *Small* **2023**, *19*, 2302479.

[34] Luo, X. X.; Xie, H.; Ma, Y.; Lan, D.; Wu, G. L.; Jia, Z. R. Advances in Fe-based electromagnetic wave absorbers: Multiscale engineering from atomic defects to macroscopic architectures for performance optimization. *Int. J. Miner. Metall. Mater.* **2026**, *33*, 768–797.

[35] Guo, Y. Q.; Ruan, K. P.; Wang, G. S.; Gu, J. W. Advances and mechanisms in polymer composites toward thermal conduction and electromagnetic wave absorption. *Sci. Bull.* **2023**, *68*, 1195–1212.

[36] He, J. Z.; Wang, X. X.; Zhang, Y. L.; Cao, M. S. Small magnetic nanoparticles decorating reduced graphene oxides to tune the electromagnetic attenuation capacity. *J. Mater. Chem. C* **2016**, *4*, 7130–7140.

[37] Ren, X. Y.; Lan, D.; Gao, Z. G.; Zhang, S. Y.; Zhang, Y.; He, M. K.; Jia, Z. R.; Wu, G. L. Semiconductor-based electromagnetic wave absorption materials: Review and perspectives. *J. Mater. Sci. Technol.* **2026**, *255*, 236–258.

[38] Guo, Z. Q.; Lan, D.; Zhang, C. H.; Gao, Z. G.; Han, M. Y.; Shi, X. T.; He, M. K.; Guo, H.; Jia, Z. R.; Wu, G. L. "Two birds one stone" strategy to integrate electromagnetic wave absorption and self-anticorrosion in magnetic nanocomposites with double-shell hollow structure. *J. Mater. Sci. Technol.* **2025**, *220*, 307–319.

[39] Shu, R. W.; Li, W. J.; Wu, Y.; Zhang, J. B.; Zhang, G. Y. Nitrogen-doped Co–C/MWCNTs nanocomposites derived from bimetallic metal-organic frameworks for electromagnetic wave absorption in the

X-band. *Chem. Eng. J.* **2019**, *362*, 513–524.
[40] Zhao, W. X.; Guo, Z. Q.; Lan, D.; Jia, Z. R.; Zhang, S. Y.; Wu, G. L. Construction of multicomponent bimetallic MOF-derived transition metal sulfide composites for electromagnetic wave absorption. *Small* **2025**, *21*, e09339.
[41] Zhang, W. L.; Xu, S.; Li, X.; Yin, Y. H.; Sun, C. L.; Yu, Z. L.; Zhao, C.; Lan, D.; Jia, Z. R.; Wu, G. L. et al. Mesoporous hollow carbon spheres/nanofibers anchored with conductive bimetallic for efficient microwave absorption. *Rare Met.* **2026**, *45*, 270051.
[42] Zhao, B.; Li, Y.; Zeng, Q. W.; Fan, B. B.; Wang, L.; Zhang, R.; Che, R. C. Growth of magnetic metals on carbon microspheres with synergetic dissipation abilities to broaden microwave absorption. *J. Mater. Sci. Technol.* **2022**, *107*, 100–110.
[43] Niu, R. F.; Jia, Z. R.; Lan, D.; Zhang, S. H.; Gao, Z. G.; Weng, Z. H.; Bai, F. R.; Wu, G. L. Heterointerface engineering of bimetallic sulfides for augmented polarization loss with electromagnetic wave absorption. *Nano Res.* **2026**, *19*, 94908411.
[44] Han, Y. X.; Yang, Y. R.; Li, T. H.; Zhang, Y. L.; Guo, H.; He, M. K.; Han, K. H.; Qiu, H.; Gu, J. W. Hierarchical heterogeneous co-based magnetic absorbers for superior broadband high-efficiency microwave absorption. *Adv. Funct. Mater.* **2026**, *36*, e25719.
[45] Zheng, J. J.; Cheng, L.; Zhang, S. J.; Lan, D.; Zhao, X. M.; Liu, X.; Zhou, J. G.; Cai, S. C.; Niu, L. Y.; Wu, G. L. et al. Harnessing decoupling and synergy between hollow structures and dual schottky contacts for electromagnetic wave absorption. *J. Mater. Sci. Technol.* **2026**, *264*, 163–172.
[46] He, M. K.; Zhong, X.; Lu, X. H.; Hu, J. W.; Ruan, K. P.; Guo, H.; Zhang, Y. L.; Guo, Y. Q.; Gu, J. W. Excellent low-frequency microwave absorption and high thermal conductivity in polydimethylsiloxane composites endowed by hydrangea-like CoNi@BN heterostructure fillers. *Adv. Mater.* **2024**, *36*, 2410186.
[47] Jia, Z. R.; Li, J. J.; Lan, D.; Zhang, S. Y.; Gao, Z. G.; Shi, X. T.; Wu, G. L. Hierarchical fiber composites assembled from MOF-derived hollow polyhedral for electromagnetic wave absorption. *J. Mater. Sci. Technol.* **2026**, *256*, 246–255.
[48] Li, X. P.; Luo, J. H.; Wang, Q. B.; Liu, X.; Huang, Z. T.; Xia, P. Y.; Wu, Y. H.; Dai, Z. Y.; Li, X. C. Synchronously formed hetero- and hollow core-branch nanostructure toward wideband electromagnetic wave absorption. *Small* **2024**, *20*, 2404609.
[49] Guo, Y. Q.; Li, P.; Zhao, R. L.; Gu, J. W. Preparation and mechanism of thermally conductive polyimide phase change composites with electromagnetic wave-absorbing performance. *Acta Polym. Sin.* **2025**, *56*, 2347–2360.
[50] Nie, Y. J.; Liu, J. X.; Zhu, H. H.; Chen, H.; Zhou, W. A novel biomass-derived carbon@ZnO@ZnSe composites for efficient electromagnetic wave absorption. *Mater. Sci. Eng. B* **2024**, *309*, 117628.
[51] Li, Q. Y.; Liu, L. Y.; Zhang, Q.; Kimura, H.; Hou, C. X.; Li, F. S.; Xie, X. B.; Sun, X. Q.; Zhang, J.; Wu, N. N. et al. Heterogeneous interfaces in 3D interconnected networks of flower-like 1T/2H molybdenum disulfide nanosheets and carbon-fibers boosts superior EM wave absorption. *J. Colloid Interface Sci.* **2024**, *671*, 67–77.
[52] Shen, Y. Q.; Zhang, F.; Zhang, Y. C.; Dang, M. M.; Li, B.; Ma, J. Q.; Du, X. Y. Ni/NiO/SiO_2/C nanofibers with strong wideband microwave absorption and robust hydrophobicity. *Appl. Surf. Sci.* **2022**, *588*, 152964.
[53] Shen, Y. Q.; Zhang, F.; Song, P. F.; Zhang, Y. C.; Zhang, T.; Wen, X. Q.; Ma, J. Q.; Zhang, D.; Du, X. Y. Design and synthesis of magnetic porous carbon nanofibers with excellent microwave absorption. *J. Alloys Compd.* **2022**, *903*, 163971.
[54] Xu, C. Y.; Luo, K. C.; Du, Y. Q.; Zhang, H. B.; Lv, X. W.; Lv, H. L.; Zhang, R. X.; Zhang, C.; Zhang, J. C.; Che, R. C. Anisotropic interfaces support the confined growth of magnetic nanometer-sized heterostructures for electromagnetic wave absorption. *Adv. Funct. Mater.* **2023**, *33*, 2307529.
[55] Wang, Y. F.; Zhou, X. H.; Han, L.; Shan, X. Y.; Cui, W. Q.; Zhu, L.; Gao, Y.; Zhai, S. R.; Lyu, L. H.; Liao, Y. P. *In-situ* growth of magnetic nanoparticles on honeycomb-like porous carbon nanofibers as lightweight and efficient microwave absorbers. *Ceram. Int.* **2023**, *49*, 35476–35487.
[56] Ma, Z. Y.; Zhao, Z. X.; Jiang, C.; Liu, Y. Q.; Ding, Z. Z.; Zhang, M. W.; Huang, S. L. Co/C and MoS_2 synergistically enhancing the electromagnetic absorption performance of silicon carbide fibers. *Appl. Surf. Sci.* **2025**, *696*, 162922.
[57] Qiu, S.; Lyu, H. L.; Liu, J. R.; Liu, Y. Z.; Wu, N. N.; Liu, W. Facile synthesis of porous nickel/carbon composite microspheres with enhanced electromagnetic wave absorption by magnetic and dielectric losses. *ACS Appl. Mater. Interfaces* **2016**, *8*, 20258–20266.
[58] Xu, X. F.; Shi, S. H.; Tang, Y. L.; Wang, G. Z.; Zhou, M. F.; Zhao, G. Q.; Zhou, X. C.; Lin, S. W.; Meng, F. B. Growth of NiAl-layered double hydroxide on graphene toward excellent anticorrosive microwave absorption application. *Adv. Sci.* **2021**, *8*, 2002658.
[59] Du, X.; Yan, F. F.; Cheng, M. T.; Li, H. Y.; Peng, C.; Liu, Y. L.; Liu, D.; Lan, D.; Wu, G. L.; Jia, Z. R. Dual-functional core-shell composites: Integrated microwave absorption and thermal management properties. *Int. J. Miner. Metall. Mater.* **2026**, *4*, 1320–1328.
[60] Lan, D.; Li, H. F.; Wang, M.; Ren, Y. J.; Zhang, J.; Zhang, M. Q.; Ouyang, L. X.; Tang, J.; Wang, Y. Y. Recent advances in construction strategies and multifunctional properties of flexible electromagnetic wave absorbing materials. *Mater. Res. Bull.* **2024**, *171*, 112630.
[61] Hao, X. R.; Ji, H. W.; Xu, L. X.; Cheng, Z. H.; Dang, C. B.; Wang, R. R.; Yue, C. X. Preparation of MOF-based superhydrophobic composite coatings with anti-corrosion and self-cleaning properties. *Surf. Coat. Technol.* **2025**, *516*, 132691.
[62] Lv, H. L.; Yao, Y. X.; Li, S. C.; Wu, G. L.; Zhao, B.; Zhou, X. D.; Dupont, R. L.; Kara, U. I.; Zhou, Y. M.; Xi, S. B. et al. Staggered circular nanoporous graphene converts electromagnetic waves into electricity. *Nat. Commun.* **2023**, *14*, 1982.
[63] Zheng, C. L.; Ning, M. Q.; Zou, Z.; Lv, G. G.; Wu, Q.; Hou, J. H.; Man, Q. K.; Li, R. W. Two birds with one stone: Broadband electromagnetic wave absorption and anticorrosion performance in 2-18 GHz for Prussian blue analog derivatives aimed for practical applications. *Small* **2023**, *19*, 2208211.
[64] Yin, P. F.; Lan, D.; Yuan, Z.; Wang, R.; Zhang, Y.; Sun, X. Y. Interface-engineered biochar/ZnO/$FeNi_3$ nanocomposite for enhanced microwave absorption and antibacterial performance. *J. Alloys Compd.* **2025**, *1037*, 182260.
[65] Li, X.; Liu, J. K.; Jia, Z. R.; Lan, D.; Ai, D.; Gao, Z. G.; Bai, F. R.; Wu, G. L. Schottky heterojunctions enabling enhanced interfacial polarization for high-performance electromagnetic wave absorption. *J. Mater. Sci. Technol.* **2026**, *268*, 41–50.
[66] Liu, P. B.; He, Z. Z.; Li, X. C.; Ding, L. F.; Liu, S. H.; Kong, J. Multifunctional hollow carbon microspheres enable superior electromagnetic wave response and corrosion barrier. *Adv. Mater.* **2025**, *37*, 2500646.
[67] Shokrani Havigh, R.; Mahmoudi Chenari, H. A comprehensive study on the effect of carbonization temperature on the physical and chemical properties of carbon fibers. *Sci. Rep.* **2022**, *12*, 10704.